An energy-resolved atomic scanning probe

Daniel Gruss,[1, 2, 3] Chih-Chun Chien,[4] Massimiliano Di Ventra,[5] and Michael Zwolak[1, *]

[1]*Center for Nanoscale Science and Technology, National Institute of Standards and Technology, Gaithersburg, MD 20899*
[2]*Maryland Nanocenter, University of Maryland, College Park, MD 20742*
[3]*Department of Physics, Oregon State University, Corvallis, OR 97331*
[4]*School of Natural Sciences, University of California, Merced, CA 95343*
[5]*Department of Physics, University of California, San Diego, CA 92093*

The density of states is a concept that is ubiquitous in classical and quantum physics, since it quantifies the energy distribution of states available in a system. Spectroscopic means allow its measurement over the entirety of a system's energy spectrum, but do not generally provide spatial resolution. Moreover, scanning probes measure the density of states locally at the position of the probe tip, but typically do not have access to the whole spectrum. Here, we show how the *local* density of states over the *whole* energy spectrum can be measured in atomic gases. This probe provides a simple, yet quantitative operational definition of a local density of states for both interacting and non-interacting systems as the rate at which particles can be siphoned from the system of interest by a narrow energy band of non-interacting states. We demonstrate that ultra-cold atomic lattices are a natural platform for implementing this concept and visualize the energy and spatial dependence of the atom density in inhomogeneous, interacting lattices.

Ultra-cold atomic lattices are increasingly employed in the simulation of many-body phenomena [1–5]. Additionally, the scanning tunneling and atomic force microscopes [6, 7] are arguably the most versatile instruments for probing materials, molecules, structures, and devices. From imaging surface defects to probing local electronic structure to testing novel devices [8], they have given the means to comprehend structures and behavior at their most basic level. Increasingly, tunable atomic-based systems that mimic, e.g., materials and electronics have been used to probe physical behavior in a way not possible with traditional techniques. In this direction, recent experimental work demonstrated the expansion of an atomic cloud [9], transport of quantum correlations and phase coherence [10], and the presence of quantum effects in neutral matter transport [11, 12]. This approach holds great promise in advancing our understanding of the natural world, especially many-body and out-of-equilibrium behavior.

In this Article, we give the local density of states (LDOS) an operational definition in terms of the rate at which particles can be distilled from a many-body system at a specific energy. The basic premise is that for a system to sustain a current into a narrow band reservoir, it must have a finite density of states at that energy. We show how to implement this approach and apply it to many-body systems. As we seek to harness and control quantum behavior for a new generation of technologies, such as quantum computers [13], spintronic devices [14], and beyond, this approach to quantifying physical phenomena will yield an unprecedented level of detail and help to determine the underlying theoretical description of many strongly interacting systems.

* Contact: mpz@nist.gov

Results

Measurement of the local density of states. We start by recalling the operation of the scanning tunneling microscope (STM) to measure the LDOS, $D(\mu)$, at frequency μ, in some region of a surface. For a typical measurement, the tip distance is held constant while the sample bias, $-V$, is changed, leading to a steady-state current given by [15–17]

$$I \approx I_0 \int_{-eV/\hbar}^{0} D(\omega)d\omega. \tag{1}$$

The LDOS is found from the differential conductance,

$$D(\mu) \propto \left.\frac{dI}{dV}\right|_{eV/\hbar=\mu}. \tag{2}$$

It is well known that this expression neglects the voltage dependence of the electronic transmission from tip to sample. Interpretational issues notwithstanding, this limits the accurate extraction of the native electronic density of states to the linear response regime, as not all changes in the current are due to changes in the LDOS. In particular, when the system has strong many-body interactions, such as a poorly screened electronic impurity, the applied bias will disturb the natural state of the surface by disrupting the nearby electron density.

Here, we suggest that these effects can be limited by an alternative setup. Rather than increasing an applied bias, to interrogate the many-body system, $\mathcal{S}$, we propose to use a narrow band probe, $\mathcal{P}$, that scans in energy. In a paradigmatic, one-dimensional setup, the current into a narrow reservoir of bandwidth $4\omega_{\mathcal{P}}$ at a frequency offset μ is proportional to the LDOS (how many particles at a given frequency),

$$I \approx -2e\omega_{\mathcal{P}} \int_{\mu-2\omega_{\mathcal{P}}}^{\mu+2\omega_{\mathcal{P}}} D(\omega)d\omega \approx -8e\omega_{\mathcal{P}}^2 D(\mu), \tag{3}$$
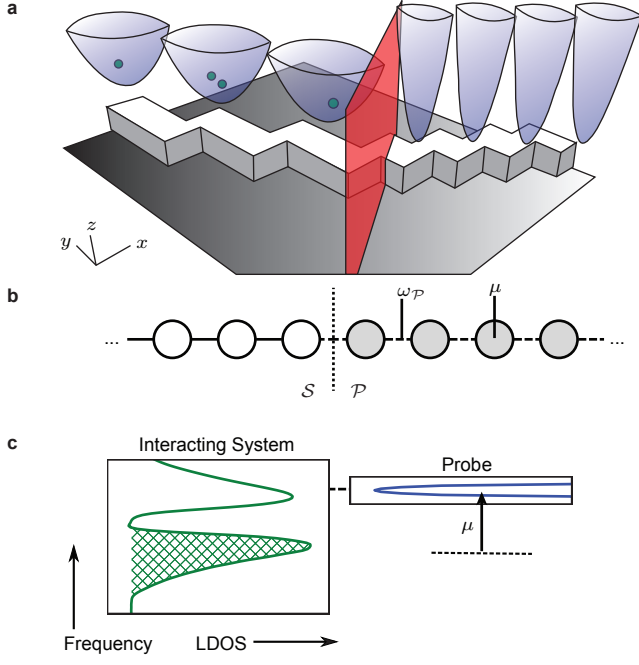
FIG. 1. **Energy-resolved atomic scanning probe.** To measure the many-body LDOS, an interacting system, $\mathcal{S}$, is placed in contact with a non-interacting, narrow band probe, $\mathcal{P}$. (**a**) The cold-atom traps are fabricated via a controlled geometry of patterned magnets, which determine the spatially-inhomogeneous coupling rates and trapping frequencies. A laser sheet (red) is initially present to prevent the flow of atoms from $\mathcal{S}$ to $\mathcal{P}$ until a measurement is performed. (**b**) This system is modeled by a 1D lattice with inhomogeneous hopping rates and onsite frequencies in $\mathcal{S}$ and $\mathcal{P}$. (**c**) A representation of the setup in frequency space shows the narrower range of frequencies and offset, μ, of the probe.

so long as $\omega_{\mathcal{P}}$ is small relative to variations of $D(\omega)$. Both empty and filled states can be probed in this way by changing the filling of $\mathcal{P}$. This setup requires tunability of $\mathcal{P}$: Its chemical potential, occupation, bandwidth/hopping, and contact magnitude/location with $\mathcal{S}$ need to be adjustable without compromising its non-interacting behavior. In other words, this setup is naturally suited to the capabilities provided by ultra-cold atoms in artificial lattice potentials. A schematic of a magnetically trapped implementation of this setup is shown in Fig. 1.

Hamiltonian. The Hamiltonian, H, for this setup is

$$H_{\mathcal{S}} + H_{\mathcal{C}} - \hbar\omega_{\mathcal{P}} \sum_{i \in \mathcal{P}} \left(c_i^\dagger c_{i+1} + \text{h.c.} \right) + \hbar\mu \sum_{i \in \mathcal{P}} c_i^\dagger c_i, \quad (4)$$

where $\omega_{\mathcal{P}}$ and μ are the hopping and *relative* onsite frequencies, respectively (i.e., the trapping frequencies for a cold-atom system, which can be controlled via magnetic potentials) and $c_i^\dagger$ (c_i) are the creation (annihilation) operators of site i. $H_{\mathcal{S}}$ is the many-body Hamiltonian of $\mathcal{S}$. $H_{\mathcal{C}}$ is the contact Hamiltonian between $\mathcal{S}$ and $\mathcal{P}$, which we also take to having hopping frequency $\omega_{\mathcal{P}}$, which gives
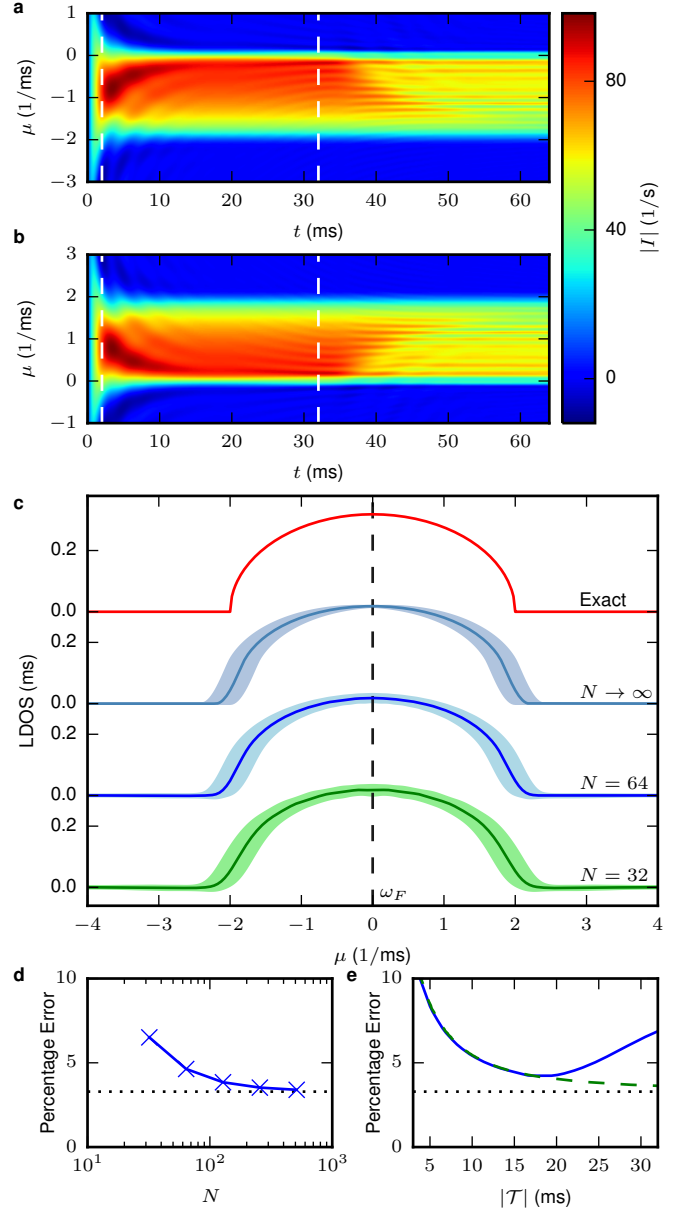

FIG. 2. **Non-interacting fermionic LDOS.** The magnitude of the current for the (**a**) occupied $\mathcal{S}$ states—using an initially empty $\mathcal{P}$—and (**b**) unoccupied $\mathcal{S}$ states—using an initially filled $\mathcal{P}$—in a 1D lattice as a function of μ, the shift in onsite frequency of $\mathcal{P}$, and the time t. Here, the total lattice length, N, is 64, the bandwidth of the probe is 400 s^{-1}, and the dotted lines indicate the region averaged for the current, $t \in \mathcal{T} = [2 \text{ ms}, 32 \text{ ms}]$ (to minimize the influence of transient currents and edge effects). (**c**) The LDOS for $\mathcal{S}$ determined from the average current and Eq. (3) (displayed with an offset for clarity). The shaded regions represent the error calculated using the standard deviation of the current in the region $\mathcal{T}$ combined with a broadening error of size $2\omega_{\mathcal{P}}$. The Fermi level, ω_F, is at the crossover point of the two measurements. (**d**) Integrated error of the LDOS versus total lattice size and (**e**) versus averaging time, $|\mathcal{T}|$, (blue solid line is $N = 32$, green dashed line is $N = 512$). The baseline error (when $N \to \infty$, the dotted line in (**d**) and (**e**)) is set by the finite $\omega_{\mathcal{P}} = \omega_{\mathcal{S}}/10$, which broadens the actual LDOS (see Eq. (20) in the Methods). For short lattices and times, the error in the LDOS is already small. Thus, even modest cold-atom systems or numerical many-body calculations can effectively reconstruct the LDOS.
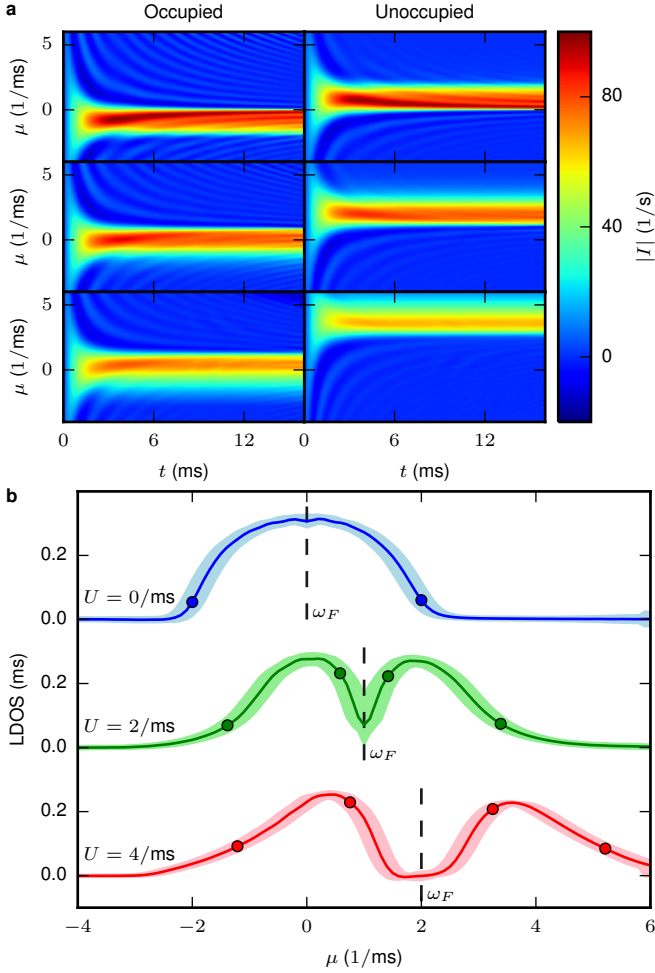
FIG. 3. **Many-body fermionic LDOS.** The time-dependent current was found using numerical many-body calculations for the (**a**) occupied and unoccupied states of a 1D lattice with a constant onsite interaction term $U_i = 0$ ms^{-1}, 2 ms^{-1}, 4 ms^{-1} (from top to bottom), and total size $N = 32$. (**b**) The resulting LDOS for $U \in \{0$ ms^{-1}, 2 ms^{-1}, 4 ms$^{-1}\}$, displayed with an offset for clarity, using the same averaging procedure as performed as in Fig. 2, with the shaded regions indicating the standard deviation of the current combined with the probe broadening error. Note that a steady-state still forms as the system ceases to be a true insulator once it is connected to the non-interacting probe. As U increases, a gap forms between the occupied and unoccupied bands, in addition to causing a pronounced broadening of both of the bands. The dots on the figure indicate the extent of the bands as found using a mean-field approximation (see Eq. (13) in the Methods).

a weak contact to a narrow band.

A laser sheet prevents contact between $\mathcal{S}$ and $\mathcal{P}$ while they are loaded with atoms and cooled to their independent ground states. One can also excite $\mathcal{S}$ by a quench or some other process; the operational definition of the LDOS also extends its applicability to nonequilibrium conditions, in addition to many-body systems. At $t = 0$, the sheet is removed. Then the composite system evolves,
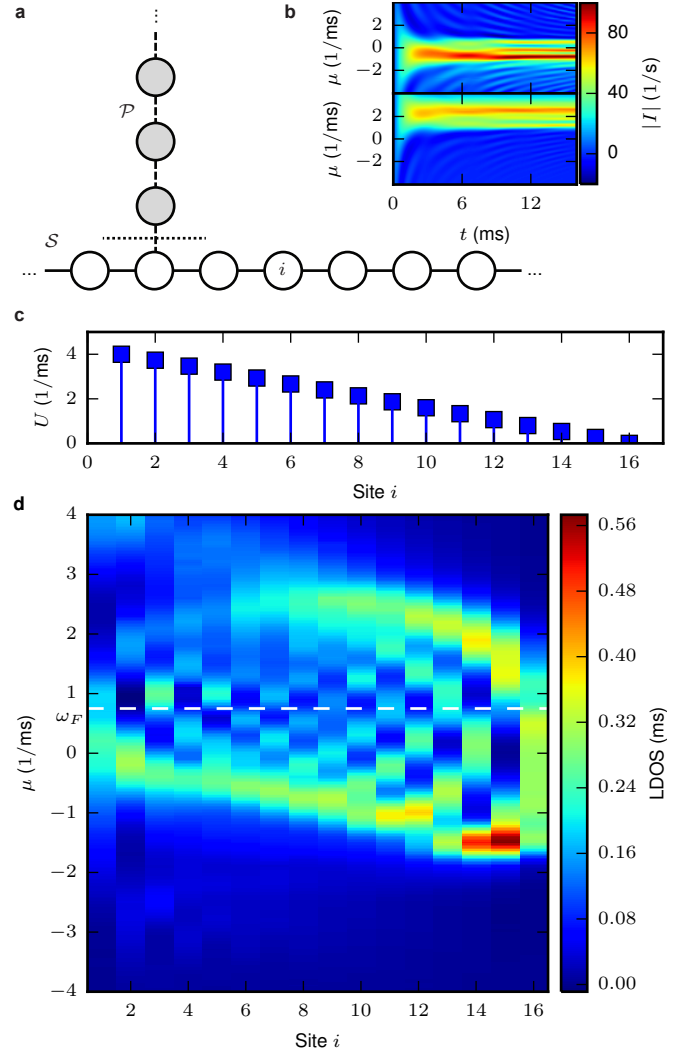

FIG. 4. **The "scanning-mode" operation of the energy resolved probe.** (**a**) Perpendicular geometry with $\mathcal{S}$ as the interacting system and $\mathcal{P}$ as the probe. The LDOS calculation was repeated for each site $i \in \mathcal{S}$. (**b**) The time-dependent current shows the formation of a steady-state flow into $\mathcal{P}$ when attached to the center of $\mathcal{S}$. (**c**) $\mathcal{S}$ has an inhomogeneous interaction profile: a linear decrease from $U = 4$ ms^{-1} on one end to $U = 0$ ms^{-1} on the other. (**d**) The LDOS for occupied and unoccupied states as a function of frequency offset μ and contact lattice position i. The weakly-interacting region of the system allows more particles to occupy lower frequency states, while the more strongly-interacting side forces the open states well beyond the Fermi level. In addition, a superimposed even-odd effect is visible, which is due to the finite size of the lattice, creating oscillations from the boundary.

giving rise to the current I, which yields the LDOS at frequency μ according to Eq. (3). The measurement is repeated for each μ of interest.

As noted above, the experimental realization of this approach requires tunability of the hopping frequencies (the probe bandwidth) and the onsite frequencies (the probe offset), among other parameters. The trap depth
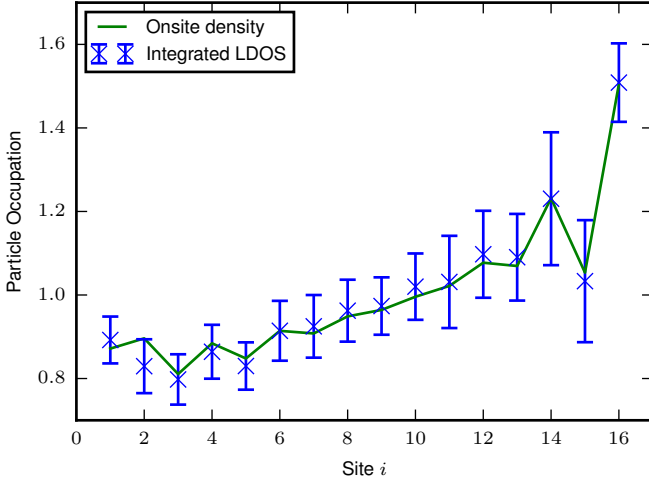
FIG. 5. **Local particle occupation.** The integral of the measured LDOS from Fig. 4 (blue x's) below the Fermi level gives the total particle occupation, which matches that found from a direct measurement of n, the occupation number, from the numerical calculation of the ground state (green line). The formation of a steady state current then provides not only a measure of the occupied and unoccupied states but also yields the real space occupation. The error bars represent the propagated error from the broadening and standard deviation as in the previous figures.

and spacing control the hopping and this can be tuned via the magnitude of the trapping potential. The onsite frequency is related to the ground state of each well, which can be modified by controlling the shape of the potential in each well. This potential can be created by atom chips with magnetic fields generated by patterned circuits of magnetic materials [18–21] or through spatial light modulation (SLM) techniques [22–24], as illustrated in Fig. 1. In $\mathcal{S}$, the interactions can be controlled by using a Feshbach resonance [25] to alter the scattering length, allowing for simulation of different types of many-body systems, such as spatially inhomogeneous or varying strength interactions (all the way down to the non-interacting limit). By engineering a series of magnetic potentials with differing onsite energies and contact locations, one can measure the LDOS as a function of frequency at any location within $\mathcal{S}$.

Non-interacting LDOS. With this method, we examine a system of interest with Hamiltonian

$$H_{\mathcal{S}} = -\hbar\omega_{\mathcal{S}} \sum_{i\in\mathcal{S},\sigma} \left(c_{i,\sigma}^\dagger c_{i+1,\sigma} + \text{h.c.} \right) + \hbar \sum_{i\in\mathcal{S}} U_i n_{i,\uparrow} n_{i,\downarrow},$$
(5)

where $\omega_{\mathcal{S}}$ is the characteristic tunneling frequency, $n_{i,\sigma} = c_{i,\sigma}^\dagger c_{i,\sigma}$ is the number operator, and U_i is the interaction frequency. The two components may refer to the spins of electrons or internal states of ultracold atoms. When inter-spin interactions are present, $H_{\mathcal{P}}$ is expanded in a similar manner to include spin. For numerical calculations, we use $\omega_{\mathcal{S}} = 1 \text{ ms}^{-1}$, a typical cold-atom tunneling

frequency [5].

We first examine a spin-polarized, non-interacting system $\mathcal{S}$: $U_i = 0$ for all i, which can be both solved exactly for the current [26, 27] and the result compared to the exact LDOS (see the Methods). Figure 2c shows the reconstruction of the LDOS using a finite lattice and time average. There is quantitative agreement between the exact LDOS and that from the energy-resolved probe (using Eq. (3)). The dominant source of error in the LDOS is the finite probe bandwidth $\omega_{\mathcal{P}}$, not the length of the lattice or the time of the average (Fig. 2d and e). This demonstrates that cold-atom systems or many-body simulations are well suited to implement this method, even though they are limited to finite lengths and times. As the total lattice length, $N \to \infty$, the averaging time, $|\mathcal{T}| \to \infty$, and the probe bandwidth, $\omega_{\mathcal{P}} \to 0$ (in this order), the exact LDOS would be recovered.

Many-body LDOS. We now apply the same approach to an interacting system with a constant $U_i = U$. Figure 3 shows the LDOS of a Mott-insulator like state. As the interaction strength increases, the band splits and a gap forms between the occupied and unoccupied bands, as is typical for a Mott insulator. However, the Fermi frequency, $\omega_F \approx U/2$, and the occupied band is shifted to higher frequency. The observations also agree with predictions from Green's function calculations in the hopping-only and interaction-only limits (see the Methods). In Ref. [28], it was found that there is a filling-dependent, conducting-to-nonconducting transition as a function of U for interacting-induced transport: An inhomogeneous quench in U, where the interaction strength is taken from 0 to a finite value for half the lattice, drives particles from that half of the lattice to the other (non-interacting) half so long as U is not too strong and the filling not too large. Figure 3b demonstrates that it is this shift of the occupied bands to higher frequency that aligns occupied states in the interacting side to open states in the non-interacting side, allowing particles to flow. As U is increased further, eventually only the tail of the occupied band is aligned with open states, thus giving a decreasing—but nonzero—current solely due to many-body interactions.

When the spatial dependence of the density of states is of interest, the probe can be used in a regime analogous to a "scanning-mode": The probe can be coupled to the system at any point along its length through a right angle construction, as shown in Fig. 4a. Examining a system with spatially inhomogeneous interactions—e.g., a linear decrease in the interaction strength U, Fig. 4b—can determine both how the particle density shifts in space and energy. Figure 4c shows the occupied and unoccupied LDOS of this inhomogeneous lattice as a function of position. The spatial decrease of the interactions forces particles to the region with small interactions, where at the very end the lattice has an LDOS similar to a non-interacting system. Just near the non-interacting boundary, however, a large peak in occupied density of states forms, i.e., states pinned well below the Fermi level. On

the interacting side, the number of particles is small with an LDOS just below the Fermi level. A superimposed even-odd effect is visible, which is due to finite lattice effects, creating oscillations away from the boundaries. There is a direct correspondence between the particle occupation and the integrated occupied LDOS, as shown in Fig. 5.

Discussion

We conclude by noting that the density of states is a central concept in our description of matter. We have provided an operational definition of the LDOS for many-body systems, applicable to in- and out-of-equilibrium cases, fermionic or bosonic systems, etc. The core principle is that for a current to flow—whether in a steady state or not—into an empty, narrow probe band, there must be occupied states at that energy (similarly for a full narrow band and unoccupied states). The measurement is resolved in both energy and space, as well potentially in other characteristics (e.g., spin-resolved). We demonstrate that a cold-atom setup will allow for the measurement of this operational definition: The many-body LDOS can be extracted with minimal disturbance to the system. While cold-atom systems allow for tunability, issues still can arise regarding, e.g., the orbital character of the local states and higher energy excitations. Unlike solid-state systems, however, the effect of these issues can be reduced in this setup.

A related approach, where tunable cold-atom systems are used to more controllably—i.e., with less disturbance to the native state—implement Eqs. (1) and (2), is also beneficial, but the narrow band setup we propose minimizes the total current flowing and all other disturbances, more so than that of the STM. The energy-resolved atomic scanning probe will complement the quantum-gas microscope [29], which resolves the spatial location of atoms. Moreover, there is also recent interest in using quantum gases to simulate the physics of the early universe [30, 31], for which the energy-resolved probe can help shed light on the nature of high-energy excitations and symmetry breaking. The ability to probe—both experimentally and numerically—the undisturbed density and occupation of states as a function of energy and position illuminates the structure of many-body systems and will help advance the theoretical description of underlying physical processes.

Methods

Non-interacting LDOS. The non-interacting lattice is exactly solvable for both the current and the LDOS. For the current, we need the retarded Green's function for a semi-infinite, one-dimensional lattice with onsite frequency μ and hopping frequency $\omega_{\mathcal{P}}$, which is [27, 32]

$$g_{\mathcal{P}}^r(\omega) = \frac{1}{2\omega_{\mathcal{P}}^2}\left[(\omega - \mu) - \imath\sqrt{4\omega_{\mathcal{P}}^2 - (\omega - \mu)^2}\right]. \quad (6)$$

Using this expression, the current for the infinite lattice, $N \to \infty$, is given by the Landauer formula [33],

$$I = -\frac{e}{2\pi}\int_{-\infty}^{\infty} d\omega\left[f_{\mathcal{S}}(\omega) - f_{\mathcal{P}}(\omega)\right]T(\omega), \quad (7)$$

where $f_{\mathcal{S}(\mathcal{P})}$ are the initial particle distributions (Fermi-Dirac distributions or completely filled/empty) in $\mathcal{S}(\mathcal{P})$ and $T(\omega)$ is the transmission coefficient

$$T(\omega) = \frac{4\,\mathrm{Re}\left[\sqrt{4\omega_{\mathcal{P}}^2 - (\omega - \mu)^2}\right]\mathrm{Re}\left[\sqrt{4\omega_{\mathcal{S}}^2 - \omega^2}\right]}{\left|\mu + \imath\sqrt{4\omega_{\mathcal{P}}^2 - (\omega - \mu)^2} + \imath\sqrt{4\omega_{\mathcal{S}}^2 - \omega^2}\right|^2}. \quad (8)$$

Implementing the setup with $f_{\mathcal{P}}(\omega) \in \{0, 1\}$ gives the reconstructed LDOS as simply a sum of the occupied and unoccupied states, and also directly yields the Fermi level, ω_F. In the main text, the system of interest $\mathcal{S}$ is half filled and in its zero temperature ground state. Here, we show, for simplicity, how the LDOS of a fully filled non-interacting system can be mapped out. The current in this case is $I = \frac{-e}{2\pi}\int_{\mu-2\omega_{\mathcal{P}}}^{\mu+2\omega_{\mathcal{P}}} T(\omega)d\omega \approx -(2/\pi)e\omega_{\mathcal{P}}T(\mu)$ when $\omega_{\mathcal{P}} \ll \omega_{\mathcal{S}}$. Thus,

$$I \approx -\frac{4}{\pi}e\left(\frac{\omega_{\mathcal{P}}}{\omega_{\mathcal{S}}}\right)^2\sqrt{4\omega_{\mathcal{S}}^2 - \mu^2} \quad (9)$$

for $|\mu| \lesssim \omega_{\mathcal{S}}$. Then Eq. (3) gives the exact LDOS, $D_{\mathrm{ex}}(\mu) = \sqrt{4\omega_{\mathcal{S}}^2 - \mu^2}/(2\pi\omega_{\mathcal{S}}^2)$, for a non-interacting $\mathcal{S}$. The remaining terms in the full expression broaden the reconstructed LDOS by approximately the probe bandwidth, $4\omega_{\mathcal{P}}$, which thus has to be small enough to discriminate features in the LDOS of $\mathcal{S}$ and, when using a cold-atom setup, the bandwidth should be large enough to get an appreciable current.

The local density of state (LDOS) is defined as [34]

$$D(\mathbf{r}, \omega) = \sum_n |\langle\mathbf{r}|\phi_n\rangle|^2\delta(\omega - \omega_n). \quad (10)$$

Here, $|\phi_n\rangle$ is the n-th eigenfunction of the full Hamiltonian with eigenvalue ω_n (in units of $\hbar$). For systems in the thermodynamic limit, the LDOS is related to the real-space Green's function by [35]

$$D(\mathbf{r}, \omega) = -\frac{1}{\pi}\,\mathrm{Im}\left[g^r(\mathbf{r}, \mathbf{r}, \omega)\right]. \quad (11)$$

These two equations give the same expression for a noninteracting semi-infinite lattice. The energy dispersion is $\omega_k = -2\omega_{\mathcal{S}}\cos[k\pi/(N + 1)]$ and $\langle r = 0|\phi_k\rangle = \sqrt{2/(N + 1)}\sin[k\pi/(N + 1)]$ with $k = 0, 1, \cdots, N$. Thus, $(L = N + 1)$

$$D(r = 0, \omega) = \int dk\frac{2}{L}\sin^2\left(\frac{k\pi}{L}\right)\frac{L\delta(k - k_{\mathcal{S}})}{2\pi\omega_{\mathcal{S}}\sin(\frac{k\pi}{L})}$$
$$= \frac{1}{2\pi\omega_{\mathcal{S}}^2}\sqrt{4\omega_{\mathcal{S}}^2 - \omega^2}. \quad (12)$$

Here, $k_{\mathcal{S}}$ is the value when $\omega - \omega_{\mathcal{S}} = 0$ is satisfied. The Green's function is similar to Eq. (6). Explicitly, $g_{\mathcal{S}}^r(\omega) = \left(\omega - \imath\sqrt{4\omega_{\mathcal{S}}^2 - \omega^2} \right)/(2\omega_{\mathcal{S}}^2)$, so $D(r = 0, \omega) = -(1/\pi)\mathrm{Im}(g^r) = \sqrt{4\omega_{\mathcal{S}}^2 - \omega^2}/(2\pi\omega_{\mathcal{S}}^2)$. Both agree with Eq. (3) and the Landauer formula.

Mean-field approximation. The Green's function for the Hubbard model in the mean-field approximation is [35]

$$g(k, \sigma, \omega) = \frac{\omega + \mu_{\mathcal{S}} - U(1-n)}{(\omega + \mu_{\mathcal{S}} - \omega_k)(\omega + \mu_{\mathcal{S}} - U) - Un\omega_k}. \quad (13)$$

Here, we focus on the 1D case with $\omega_k = -2\omega_{\mathcal{S}}\cos(k\pi/L)$ and chemical potential $\mu_{\mathcal{S}}$. $\sigma = \uparrow, \downarrow$ denotes the chosen spin species, and n is the filling factor. The poles of the Green's function lead to the energy dispersion, which has the form $(\omega - \omega_k^-)(\omega - \omega_k^+)$ with $\omega_k^{\pm}$ giving the two bands:

$$\omega_k^{\pm} = \frac{U}{2} - \mu_{\mathcal{S}} + \frac{\omega_k}{2} \pm \sqrt{\frac{U^2}{4} + \left(n - \frac{1}{2}\right)U\omega_k + \frac{\omega_k^2}{4}}. \quad (14)$$

The retarded Green's function in real space is $g^r(r, \sigma, \omega) = \int (dk/2\pi)e^{ikr} g(k, \sigma, \omega + i0^+)$. Since the Green's function is for a uniform, translational invariant system, we may choose $r = 0$. By using the identity $1/(x + i0^+) = P(1/x) - i\pi\delta(x)$ with P denoting the Cauchy principle integral, the LDOS for one spin component is

$$D(\sigma, \omega) = -\frac{1}{\pi}\,\mathrm{Im}\,g^r(r = 0, \sigma, \omega) \quad (15)$$
$$= \sum_k [\alpha_k\delta(\omega - \omega_k^-) + (1 - \alpha_k)\delta(\omega - \omega_k^+)].$$

Here, α_k satisfies $\alpha_k(\omega_k^+ - \omega_k^-) = U(1-n)$. One may view the prefactors as the weight of wavefunctions at r and the delta functions pick the frequencies that matches the two energy bands. In the isolated-site limit where $(\omega_{\mathcal{S}}/U) \to 0$, the Green's function is exactly solvable and on a selected site it is $g_{\mathcal{S}}(\sigma, \omega) = \left[\frac{1-(n/2)}{\omega+\mu_{\mathcal{S}}} + \frac{n/2}{\omega+\mu_{\mathcal{S}}-U}\right]$. By analytic continuation $\omega \to \omega - i0^+$, we obtain $g_{\mathcal{S}}^r$. Then, $D(\sigma, \omega) = \{[1-(n/2)]\delta(\omega+\mu_{\mathcal{S}}) + (n/2)\delta(\omega+\mu_{\mathcal{S}} - U)\}$. Thus, there are two peaks at $-\mu_{\mathcal{S}}$ and $-\mu_{\mathcal{S}} + U$. Away from the isolated-site limit, the two peaks broaden into two bands separated by U, and this agrees with our observation shown in Fig. 3.

Numerical considerations and error quantification. In order to extract the LDOS from real-time measurements on finite lattices, the current must be averaged over a finite time, i.e., the current will be in a quasi-steady state [33]. The estimate of the LDOS is thus

$$D(\mu) \propto \frac{1}{|\mathcal{T}|}\int_{\mathcal{T}} I(t)dt. \quad (16)$$

As $|\mathcal{T}|, N \to \infty$, this will converge to the true steady state. As we demonstrate, already for very small lattices

an accurate LDOS can be obtained and thus only modest resources are needed.

The numerical calculations are performed as follows: For the non-interacting system, the current was found from the numerical integration of the equations of motion [26, 27]. The transient current when the probe is placed in contact with the system is damped on the characteristic tunneling time and the recurrence time is proportional to the lattice size, which determines both the lower and upper limits to the time region $\mathcal{T}$ given a finite lattice length. We use $\mathcal{T} = [2 \text{ ms}, N/2 \text{ ms}]$, where N is the lattice length. We can also define an exact error for the non-interacting case,

$$\text{Percentage Error} = 100 \% \cdot \frac{\sqrt{\int [D(\mu) - D_{\mathrm{ex}}(\mu)]^2 \, d\mu}}{\sqrt{\int D_{\mathrm{ex}}(\mu)^2 \, d\mu}}, \quad (17)$$

where $D_{\mathrm{ex}}(\mu)$ is the exact LDOS.

The uncertainty due to probe broadening is due to contributions to the current from anywhere within the probe bandwidth of $4\omega_q p$, which results in an error, $\sigma_+(\mu)$, of

$$D(\mu) - \max[D(\mu), D(\mu - 2\omega_{\mathcal{P}}), D(\mu + 2\omega_{\mathcal{P}})] \quad (18)$$

for the positive μ side and, $\sigma_-(\mu)$,

$$D(\mu) - \min[D(\mu), D(\mu - 2\omega_{\mathcal{P}}), D(\mu + 2\omega_{\mathcal{P}})] \quad (19)$$

for the negative side. This is combined with the standard deviation, σ_{stdev}, from the time-dependent current for a total error of

$$\sigma_{\mathrm{tot}}^{\pm} = \sqrt{\sigma_{\pm}^2 + \sigma_{\mathrm{stdev}}^2}. \quad (20)$$

For the interacting systems, we perform time-dependent, density matrix renormalization group calculations [36, 37] within the ITensor tensor product library [38]. In all simulations, the time step was reduced until the calculation converged with respect to energy conservation and the maximum matrix bond dimension was allowed to increase without bound. The energy cutoff was set to $10^{-9}\omega_{\mathcal{S}}$. The averaging is done in the region $\mathcal{T} = [2 \text{ ms}, N/2 \text{ ms}]$, as with the non-interacting case.

Acknowledgments

Contributions

M.Z. proposed the project, D.G. and C.C.C. performed analytical calculations and D.G. performed numerical calculations. All authors helped to clarify the ideas and wrote the manuscript.

Additional information

Correspondence and requests for material should be addressed to M.Z. (mpz@nist.gov).

Competing Interests

The authors declare no competing financial interests.

---

[1] Bloch, I., Dalibard, J. & Zwerger, W. Many-body physics with ultracold gases. *Rev. Mod. Phys.* **80**, 885 (2008).

[2] Fertig, C. *et al.* Strongly inhibited transport of a degenerate 1D bose gas in a lattice. *Phys. Rev. Lett.* **94**, 120403 (2005).

[3] Strohmaier, N. *et al.* Interaction-controlled transport of an ultracold Fermi gas. *Phys. Rev. Lett.* **99**, 220601 (2007).

[4] Lamacraft, A. & Moore, J. Potential insights into nonequilibrium behavior from atomic physics. In Levin, K., Fetter, A. L. & Stamper-Kurn, D. (eds.) *Ultracold bosonic and fermionic gases* (Elsevier, Amsterdam, The Netherlands, 2012).

[5] Chien, C.-C., Peotta, S. & Di Ventra, M. Quantum transport in ultracold atoms. *Nat. Phys.* **11**, 998–1004 (2015).

[6] Binnig, G., Rohrer, H., Gerber, C. & Weibel, E. Surface studies by scanning tunneling microscopy. *Phys. Rev. Lett.* **49**, 57 (1982).

[7] Binnig, G., Quate, C. F. & Gerber, C. Atomic force microscope. *Phys. Rev. Lett.* **56**, 930 (1986).

[8] Wiesendanger, R. *Scanning probe microscopy and spectroscopy: methods and applications* (Cambridge University Press, 1994).

[9] Ott, H. *et al.* Collisionally induced transport in periodic potentials. *Phys. Rev. Lett.* **92**, 160601 (2004).

[10] Günter, K., Stöferle, T., Moritz, H., Köhl, M. & Esslinger, T. Bose-Fermi mixtures in a three-dimensional optical lattice. *Phys. Rev. Lett.* **96**, 180402 (2006).

[11] Brantut, J.-P., Meineke, J., Stadler, D., Krinner, S. & Esslinger, T. Conduction of ultracold fermions through a mesoscopic channel. *Science* **337**, 1069–1071 (2012).

[12] Krinner, S., Stadler, D., Husmann, D., Brantut, J.-P. & Esslinger, T. Observation of quantized conductance in neutral matter. *Nature* **517**, 64–67 (2015).

[13] Ladd, T. D. *et al.* Quantum computers. *Nature* **464**, 45–53 (2010).

[14] Žutić, I., Fabian, J. & Sarma, S. D. Spintronics: Fundamentals and applications. *Rev. Mod. Phys.* **76**, 323 (2004).

[15] Hansma, P. K. & Tersoff, J. Scanning tunneling microscopy. *J. Appl. Phys.* **61**, R1–R24 (1987).

[16] Chen, C. J. *Introduction to scanning tunneling microscopy* (Oxford University Press New York, 1993).

[17] Stroscio, J. & Kaiser, W. Methods of experimental physics, vol. 27. *Scanning Tunneling Microscopy. Academic Press, Boston* (1993).

[18] Gerritsma, R. *et al.* Lattice of microtraps for ultracold atoms based on patterned magnetic films. *Phys. Rev. A* **76**, 033408 (2007).

[19] Singh, M. *et al.* One-dimensional lattice of permanent magnetic microtraps for ultracold atoms on an atom chip. *J. Phys. B: At. Mol. Opt. Phys.* **41**, 065301 (2008).

[20] Reichel, J. & Vuletic, V. (eds.) *Atom Chips* (Wiley-VCH, Weinheim, Germany, 2011).

[21] Jose, S. *et al.* Periodic array of Bose-Einstein condensates in a magnetic lattice. *Phys. Rev. A* **89**, 051602 (2014).

[22] McGloin, D., Spalding, G. C., Melville, H., Sibbett, W. & Dholakia, K. Applications of spatial light modulators in atom optics. *Opt. Express* **11**, 158–166 (2003).

[23] Pasienski, M. & DeMarco, B. A high-accuracy algorithm for designing arbitrary holographic atom traps. *Opt. Express* **16**, 2176–2190 (2008).

[24] Nogrette, F. *et al.* Single-atom trapping in holographic 2D arrays of microtraps with arbitrary geometries. *Phys. Rev. X* **4**, 021034 (2014).

[25] Chin, C., Grimm, R., Julienne, P. & Tiesinga, E. Feshbach resonances in ultracold gases. *Rev. Mod. Phys.* **82**, 1225 (2010).

[26] Chien, C.-C., Zwolak, M. & Di Ventra, M. Bosonic and fermionic transport phenomena of ultracold atoms in one-dimensional optical lattices. *Phys. Rev. A* **85**, 041601 (2012).

[27] Chien, C.-C., Di Ventra, M. & Zwolak, M. Landauer, Kubo, and microcanonical approaches to quantum transport and noise: A comparison and implications for cold-atom dynamics. *Phys. Rev. A* **90**, 023624 (2014).

[28] Chien, C.-C., Gruss, D., Di Ventra, M. & Zwolak, M. Interaction-induced conducting–non-conducting transition of ultra-cold atoms in one-dimensional optical lattices. *New J. Phys.* **15**, 063026 (2013).

[29] Bakr, W. S., Gillen, J. I., Peng, A., Folling, S. & Greiner, M. A quantum gas microscope for detecting single atoms in a Hubbard-regime optical lattice. *Nature* **462**, 74–77 (2009).

[30] Hung, C.-L., Gurarie, V. & Chin, C. From cosmology to cold atoms: observation of Sakharov oscillations in a quenched atomic superfluid. *Science* **341**, 1213–1215 (2013).

[31] Kasamatsu, K., Ichinose, I. & Matsui, T. Atomic quantum simulation of the lattice gauge-Higgs model: Higgs couplings and emergence of exact local gauge symmetry. *Phys. Rev. Lett.* **111**, 115303 (2013).

[32] Zwolak, M. & Di Ventra, M. DNA spintronics. *Appl. Phys. Lett.* **81**, 925–927 (2002).

[33] Di Ventra, M. *Electrical transport in nanoscale systems* (Cambridge University Press Cambridge, Cambridge, UK, 2008).

[34] Hedin, L., Lundqvist, B. I. & Lundqvist, S. One-electron approximation: Density of states for interacting electrons. *J. Res. Nat. Bur. Stand. Sect. A* **74A**, 417–431 (1970).

[35] Rickayzen, G. *Green's functions and condensed matter* (Dover publications, 2013).

[36] Vidal, G. Efficient classical simulation of slightly entangled quantum computations. *Phys. Rev. Lett.* **91**, 147902 (2003).

[37] Vidal, G. Efficient simulation of one-dimensional quantum many-body systems. *Phys. Rev. Lett.* **93**, 040502 (2004).

[38] Stoudenmire, E. M. & White, S. R. ITensor - Intelligent Tensor Library. http://itensor.org/. Accessed: 2016-04-06.